Direct Laser Patterning and Phase Transformation of 2D $PdSe_2$ Films for On Demand Device Fabrication

Viktoryia Shautsova,[1*] Sapna Sinha,[1] Linlin Hou,[1] Qianyang Zhang,[1] Martin Tweedie,[1] Yang Lu,[1] Yuewen Sheng,[1] Benjamin Porter,[1] Harish Bhaskaran,[1] Jamie Warner[1*]

Department of Materials, University of Oxford, Parks Road, Oxford OX1 3PH, United Kingdom

*email: viktoryia.shautsova@materials.ox.ac.uk, jamie.warner@materials.ox.ac.uk

Abstract

Heterophase homojunction formation in atomically thin 2D layers is of great importance for next-generation nanoelectronics and optoelectronics applications. Technologically challenging, controllable transformation between the semiconducting and metallic phases of transition metal chalcogenides is of particular importance. Here, we demonstrate that controlled laser irradiation can be used to directly ablate $PdSe_2$ thin films using high power, or trigger the local transformation of $PdSe_2$ into a metallic phase $PdSe_{2-x}$ using lower laser power. Such transformations are possible due to the low decomposition temperature of $PdSe_2$ compared to other 2D transition metal dichalcogenides. Scanning transmission electron microscopy is used to reveal the laser-induced Se-deficient phases of $PdSe_2$ material. The process sensitivity to the laser power allows patterning flexibility for resist free device fabrication. The laser patterned devices demonstrate that a laser-induced metallic phase $PdSe_{2-x}$ is stable with increased conductivity by a factor of about 20 compared to $PdSe_2$. These findings contribute to

the development of nanoscale devices with homojunctions and scalable methods to achieve structural transformations in 2D materials.

Keywords

2D materials, phase transformation, laser patterning, graphene, $PdSe_2$, device fabrication, FET

Two-dimensional materials with tunable band gap in the range of 0.3–1.5 eV are highly desirable for electronic and optoelectronic applications. Palladium diselenide ($PdSe_2$), a less explored group-10 transition metal dichalcogenide, is one such material of particular interest that demonstrates a gradual transition from a semiconductor (monolayer) to semimetal (bulk). [1,2] A unique anisotropic structure of $PdSe_2$ material with unusual 4-fold coordination of the metal atoms and intralayer chalcogen atom bonding results in strong interlayer interaction leading to interesting phase engineering results. [3-11] Polymorphic phases such as a layered monoclinic phase, [3] a layered 1T phase [4] or a pyrite-type phase [5] can be obtained by weakening of Se-Se intralayer bonds in high pressure environment. By introducing Se vacancies, the layered $PdSe_2$ phase can be modified into metallic phases such as $Pd_{17}Se_{15}$ [6] and Pd_2Se_3. [7,8] Furthermore, palladium-rich or selenium-rich stoichiometries of binary compounds are known to result in various different compositions facilitating new material phases. [9-11] Facilitating local phase transitions offers vast opportunities to create high quality heterophase structures with unique properties. For example, Zuluaga *et al.* has demonstrated that lateral junctions between a $PdSe_2$ bilayer and a Pd_2Se_3 monolayer result in formation of a 1D channel with smaller band gap. [8] By creating $Pd_{17}Se_{15}/PdSe_2$ junction, seamless Ohmic contacts have been formed for field effect transistors. [6]

To introduce phase modifications, variety of processing methods can be used including plasma treatment, [6] electron or ion beam irradiation [7,8] and laser exposure. [12] The laser-driven phase patterning is of particular importance due to its nanoscale features, reliability, scalability

and low cost. The phase transition is driven by laser irradiation in a desired area and thus does not require creation of predefined pattern designs. This technique has been widely employed to graphene based systems to both pattern the layers through local material ablation with pulsed lasers [13,14] and to locally reduce graphene oxide facilitating junction formation. [15-17] Laser-induced thinning has been demonstrated for MoS_2 enabling on demand fabrication of a single-layer areas from multilayers flakes. [18] Cho *et al.* has reported laser-induced phase patterning in $MoTe_2$ leading to formation of homojunction Ohmic contacts. [12]

In this work we report laser-driven phase patterning in $PdSe_2$ to realize on demand device fabrication. Laser irradiation results in material transition to the palladium-rich phase $PdSe_{2-x}$ followed by formation of Pd nanoparticles as confirmed by atomic resolution scanning transmission electron microscopy (STEM). Using STEM imaging, we identified that the formation of the Se vacancy is a most likely origin of the phase transition. With selective laser power conditions, we modified $PdSe_2$ field effect transistor devices with graphene contacts to fabricate $PdSe_{2-x}$ junctions with well-defined ablated regions. Transport measurements demonstrate significant increase in the material conductivity further supporting the formation of Pd-rich phase.

Results and Discussion

In a typical experiment, a commercial multilayer $PdSe_2$ film on a sapphire substrate is transferred onto a substrate of interest, such as a holey Si_3N_4 TEM chip or a Si/SiO_2 (300 nm) substrate. As will be discussed in details below, the $PdSe_2$ material demonstrates strong sensitivity to laser exposure (Fig. 1a), where high laser power results in local material degradation and formation of Pd nanoparticles (NPs), while lower laser power can be used to controllably modify the $PdSe_2$ phase, making it Se-deficient and resulting in a $PdSe_{2-x}$ phase. We start by studying the structural modifications in the material under laser

exposure. For this purpose, the material was transferred to TEM chips with and without a graphene supporting layer. The underlying graphene layer provides support for imaging of parts of the $PdSe_2$ film that would normally have been lost to vacuum. The schematic of the experiment is presented in Figure 1b, where the laser is positioned in the centre of TEM window. We used a confocal Raman microscope system to perform the laser annealing with minimum exposure time of 1s. The laser exposure results in local material degradation leading to hole formation that expands significantly with increasing laser power (Fig. 1 c,d). A closer inspection reveals four distinct regions within the film after laser exposure (Fig. 1 e,f): (1) hole region where the $PdSe_2$ film and graphene are fully damaged, as schematically illustrated by red colour in Fig. 1f; (2) $PdSe_2$ film is modified forming Pd NPs; (3) the phase change of the material is observed where $PdSe_2$ transforms into $PdSe_{2-x}$ and (4) unmodified area of $PdSe_2$. By varying the laser power, we identified that for graphene supported samples, material damage can be induced at 600 μW, while at 60 μW the material stays intact. Interestingly, the film without the underlying graphene support shows 10 times lower laser power threshold (60 μW) for damage and demonstrates larger sizes of the formed holes (Fig. 1g). This is consistent with thermal energy transfer to underlying graphene layer resulting in lower local temperatures within $PdSe_2$ film. [19, 20]

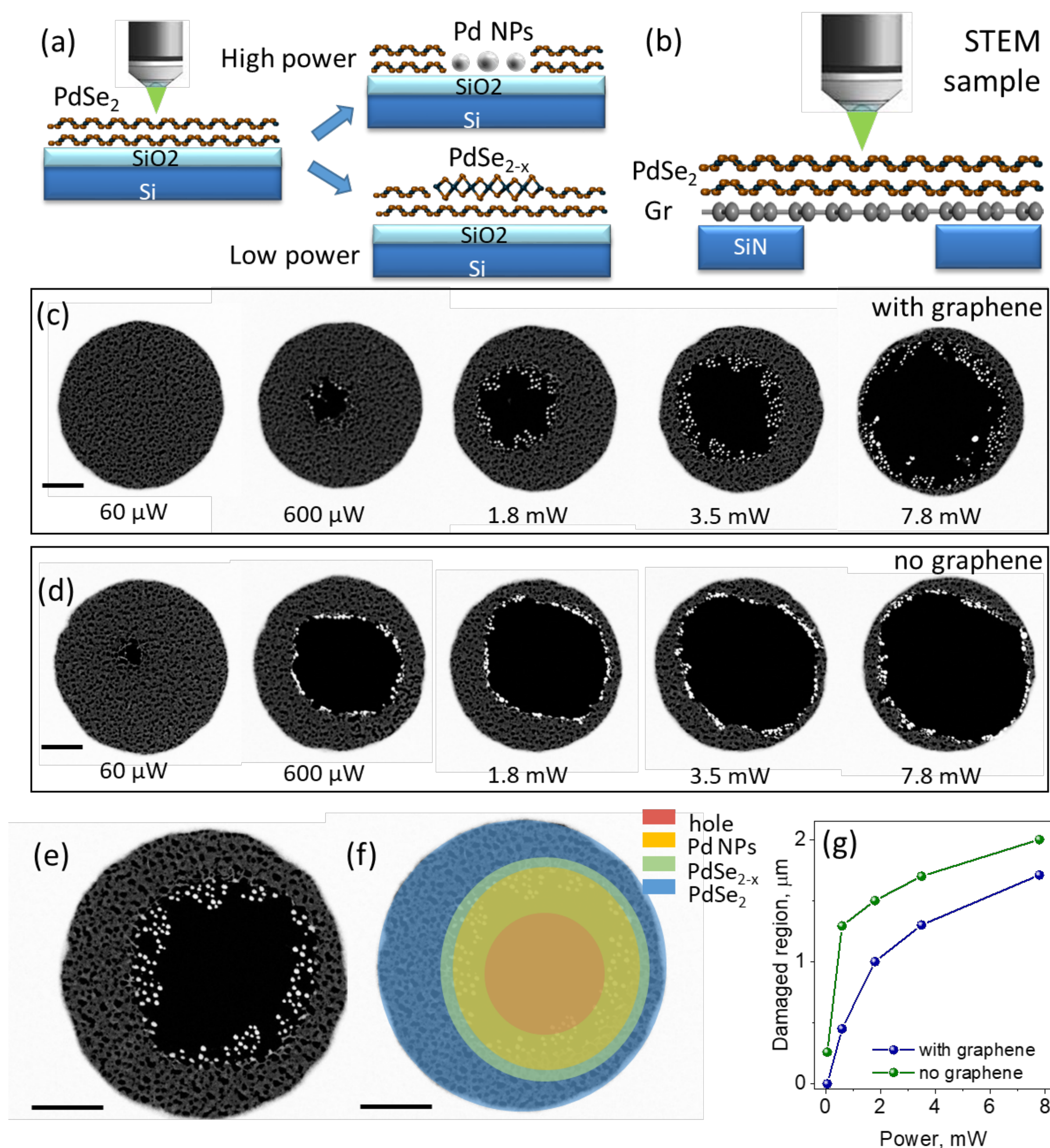

Figure 1. Laser induced modifications of $PdSe_2$. (a) Schematic representation of the $PdSe_2$ material transformation under laser exposure. (b) Schematic side view of the TEM sample geometry. (c, d) Laser induced film damage with various laser power for the samples with/without underlying graphene support. Scale bar is 500 nm. (e) TEM image of the laser annealed sample. There are four distinct regions present in the sample: (1) graphene and $PdSe_2$ film destruction resulting in a hole, (2) $PdSe_2$ destruction resulting in formation of Pd nanoparticles, (3) transformation region with $PdSe_{2-x}$ phase and (4) unaffected region with

original $PdSe_2$ phase. Different regions are schematically presented in (f). Scale bar is 500 nm. (g) Dependence of the hole size on the laser power.

Figure 2 shows the annular dark field scanning transmission electron microscopy (ADF-STEM) study of the laser irradiated $PdSe_2$ material on graphene from Figure 1c. In Figure 2a, the red boxed region indicates the edge of the laser induced hole, shown in more detail in Figure 2b, where a white line shows the boundary between two different crystal phases of the material. At the edge of the hole, Figure 2c, the material shows Pd NPs. Figure 2e-k, show the atomic resolution ADF-STEM images, multislice image simulations and FFT of pristine few layered $PdSe_2$ that is far from the laser induced hole. Figure 2l,m shows the Pd NP and FFT, from the outermost region to the right of Figure 2b, while Figure 2n-o shows the selenium deficient $PdSe_{2-x}$ phase that is found between the Pd NPs and the pristine few layer $PdSe_2$, shown in the blue box region in Figure 2c and Figure 2d. The crystal structure of $PdSe_{2-x}$ phase presented in Figure 2n, is highly defective and does not have a determinable unit cell due to the nanoscale distribution of Pd-Se bonding, but is not amorphous, as seen in the FFT of Figure 2o. Images of the sharp interface between the $PdSe_2$:$PdSe_{2-x}$ are shown in Figure 2p-t, where the FFT can identify the two phases on either side. We additionally study the $PdSe_2$ phase transformation induced under various laser exposure conditions (Supporting information S2). It is particularly interesting to analyse the large area exposure results. In this experiment, in contrast to 100x objective used in the main study, we utilised 10x objective resulting in a 5 µm laser spot. Under these conditions, the laser density is strongly reduced, while much larger area of the material is exposed to the laser power above the phase transformation threshold. Interestingly, one of the observed selenium deficient phases corresponds to $Pd_{17}Se_{15}$ recently reported for the $PdSe_2$ material treated with Ar plasma. [6] This observation indicates potential similarities in the mechanism of the material phase transformation that is driven by the defects induced during the material treatment process as discussed in details below.

We explain the observed material modifications by the following mechanism. Laser exposure introduces local heating in the material that facilitates removal of lighter Se atoms from the top layer, while the Se atoms in the middle regions are rearranged forming $PdSe_{2-x}$ structure (Fig. 2u,v). Similar process has been recently observed for controlled thermal annealing of $PdSe_2$ that results in formation of $PdSe_{2-x}$ striated phase with 1D sub-nm etched channels in Pd_2Se_3 bilayers, as discussed in our recent work. [21] In general, this process originates from extraordinary interlayer interaction between the $PdSe_2$ layers. The layer binding energy for $PdSe_2$ material of 190 meV/atom [22] is much higher compared to typical 2D materials, for example graphene and hBN demonstrating ~32 meV/atom [23] and 52 meV/atom, [24] respectively. This is because most 2D layered materials such as graphene and TMDs show only weak interlayer interaction through van der Waal forces even in the presence of defects. In fact, during the heating processes the chalcogen vacancies are typically activated in the TMDs resulting in formation of line defects and subsequently 2-dimensional holes. [25-27] In contrast, Se vacancies reduce the distance between layers causing the melding of two layers into one and thus formation of the new phase is observed. [7] Zuluaga *et al.* demonstrated that the electron beam irradiation can be used to facilitate the emission of Se atoms resulting in the transformation of bilayer $PdSe_2$ into a monolayer Pd_2Se_3 phase. [28] The local nature of e-beam induced modification of the $PdSe_2$ material facilitates fabrication of two-dimensional $PdSe_2$-Pd_2Se_3 junctions. However, this conversion process is expensive and extremely time consuming due to small size of the electron beam significantly limiting the application of this technique. Since the laser irradiation can produce similar selenium deficient modifications to the material, as well as total ablation, we further explore potential of this technique for the device fabrication where high laser power causes ablation removes material while lower power causes Se deficiency and phase changes.

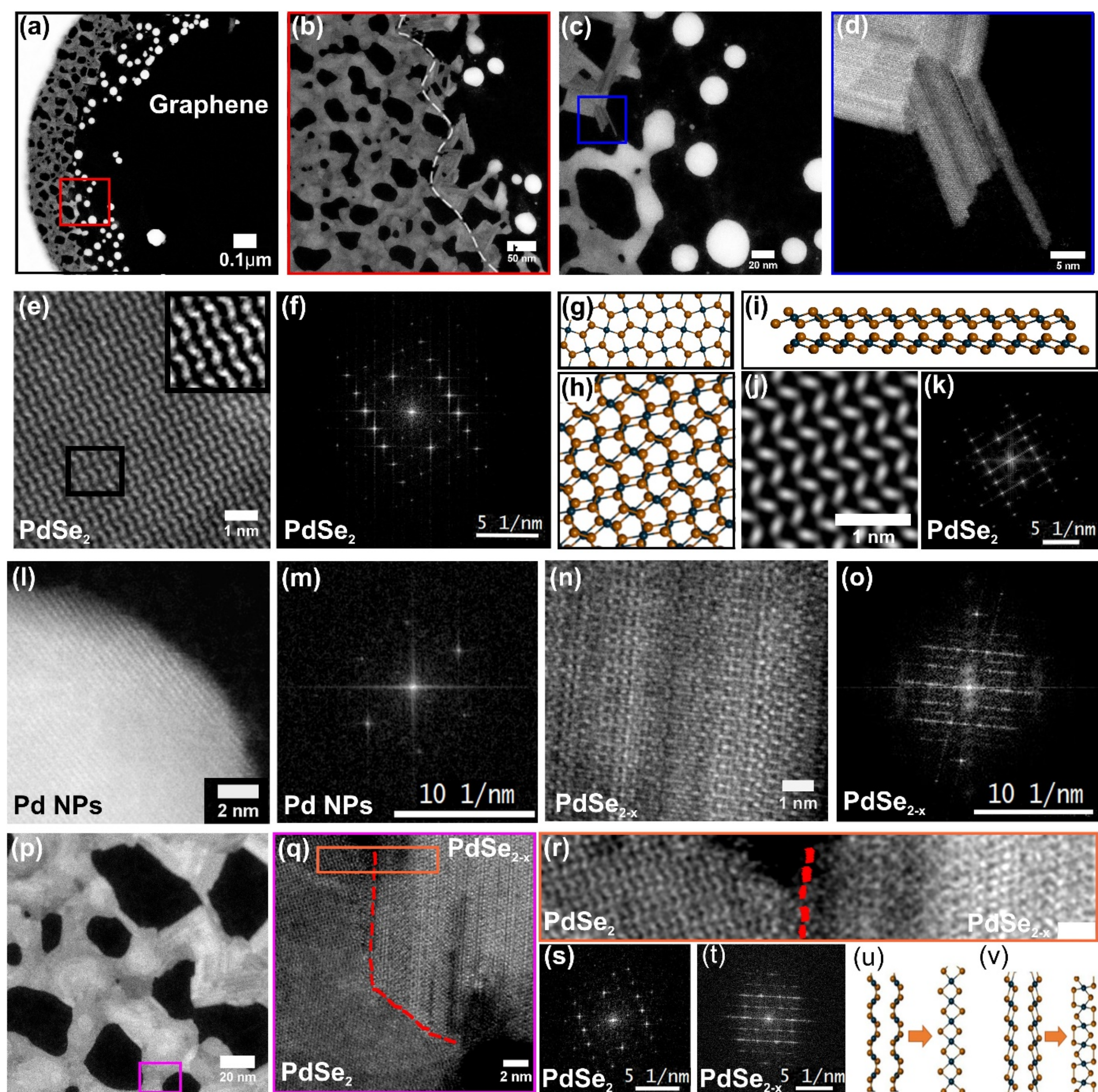

Figure 2. STEM characterization of crystal structure of $PdSe_{2-x}$ and its interface with $PdSe_2$. (a) Low magnification ADF-STEM of the sample on graphene after laser exposure (7.8 mW). (b) Magnified ADF-STEM image of the material annotated in the red box in (a), where the white line shows the demarcation between two different phases of the material. (c) Magnified ADF-STEM image of the laser-modified material, closer to the edge. (d) High resolution ADF-STEM image of the material annotated in the blue box in (c). (e) High resolution image of the initial material, which clearly shows the $PdSe_2$ structure. The inset is the atomic resolution image of the boxed region. (f) Fast Fourier transform (FFT) of (e).

(g) Top view of the atomic model of single layer $PdSe_2$. (h) Top view of the atomic model of two (even layers) $PdSe_2$. (i) Side-view of bilayer (even layers) $PdSe_2$. (j) Multislice ADF-STEM image simulation of the atomic model in (h). (k) FFT of the simulation in (l). (l) Pd nanoparticles formed after complete ejection of Se atoms (see Supporting Information S1 for the crystal analysis). (m) FFT of (l). (n) The high resolution image which clearly shows the transitioned $PdSe_{2-x}$ structure. (o) FFT of the (n). (p) Low magnification ADF-STEM image of the region transitioning from $PdSe_2$ to $PdSe_{2-x}$. (q) Magnified image of the transition material annotated in the pink box in figure p. The red line shows the grain boundary. (r) Atomic resolution of image annotated in orange box in (q). The left side shows the $PdSe_2$ structure whereas the right side shows the Se-deficient $PdSe_{2-x}$ structure. (s-t) FFT of $PdSe_2$ and $PdSe_{2-x}$ respectively, taken from the material in figure r. (u-v) Atomic model structures of possible conversions of the material from $PdSe_2$ to Se-deficient material.

Next, the $PdSe_2$ film was transferred on Si/SiO_2 (300 nm) substrate that is typically used for device fabrication (see Methods section). We start by studying the internal material sensitivity to laser exposure, which is expected to be significantly different due to presence of the underlying substrate acting as a heat sink. The laser exposure is performed using the same confocal Raman microscope. We also use this system for on-demand material modification and patterning, as discussed later in the text. While other setups such as laser pattern generators are optimised to perform fast laser-based lithography and are much more flexible with the target patterns, the Raman system provides us with additional *in situ* Raman spectra to control the process in real time.

To promote the material deformation, the $PdSe_2$ was exposed for 1 s to laser radiation with laser power varying from ~0.6 mW to ~7.8 mW, as shown on the schematic in Figure 3a. After the exposure, the material was investigated with Raman spectroscopy using much lower laser power of ~60 μW to ensure no further degradation is induced. Figure 3 (b, c) compares

the Raman spectra measured for a $PdSe_2$ before and after laser exposure. Consistent with previous reports, [2,29] $PdSe_2$ exhibits four distinct Raman peak with the most intense ones observed at 145 cm^{-1} and 260 cm^{-1}. After laser exposure, the Raman peaks undergo modifications. Interestingly, there is a negligible change in the peak positions, which is in good agreement with previous study of phase transition in $PdSe_2$ layer induced by Ar-plasma. [6] In this study, it has been demonstrated that for $PdSe_2$ film thickness of ~ 7 nm, only breathing modes located at frequencies < 100 cm^{-1} are affected by the material phase transformation. It should be noted, that breathing modes are inaccessible in the current study due to limitations of the Raman system. Additionally, the position of $PdSe_2$ Raman peaks strongly depends on the number of layers and can provide fingerprints for thickness determination. [2,30] However, for the high frequency peaks (>100 cm^{-1}) which are analysed in this study, the thickness dependence becomes weak for the $PdSe_2$ films with more than 6 layers, [2] which is the case in the current study.

In contrast, the intensity of the $PdSe_2$ peaks is drastically reduced, while the intensity of the Si peak at 520 cm^{-1} is increased. This can be explained by a reduction of the material thickness or by material degradation. To investigate this question further, AFM measurements were performed on the exposed areas. Consistent with Raman spectroscopy results, we observe no material modification for laser power of ~0.6 mW, while the laser power of ~1.8 mW results in material thinning, where ~1.7 nm is removed compared to the initial film thickness of ~5.5 nm (Supporting information S3). In contrast, the laser powers of 3.5 mW and 7.8 mW result in local degradation of the material as confirmed by particle formation. SEM results further identify strong material degradation for these high laser powers (Supporting information S4). The observed structural modifications for the supported $PdSe_2$ film are in excellent agreement with the TEM results discussed earlier. Similarly, when the threshold laser power is reached

the material undergoes strong degradation with Pd NP formation, while lower laser power results in laser-induced phase transition and thus local material thinning.

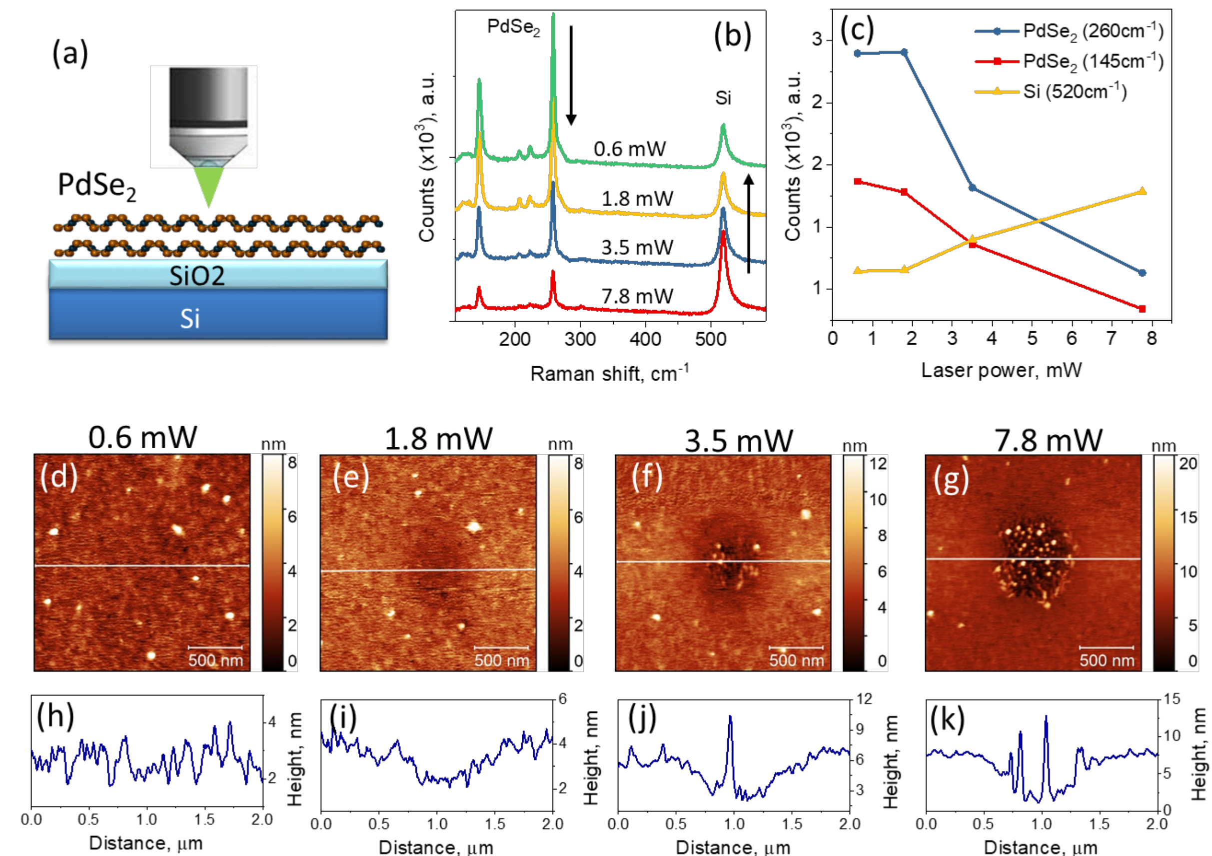

Figure 3. Laser sensitivity of supported $PdSe_2$ layer. (a) Schematic side view of the laser annealing process in a supported geometry. (b, c) Raman spectra evolution after exposure with varying laser power of 0.6, 1.8, 3.5 and 7.8 mW as probed by safe laser power of 60 μW. (d-g) AFM images of the modified $PdSe_2$ film after laser exposure with varying laser power of 0.6 mW (d), 1.8 mW (e), 3.5 mW (f) and 7.8 mW (g) and corresponding cross-sections (h-k).

Next, we further explore the possibility of using high laser power to completely remove the $PdSe_2$ film and thus produce a desired pattern. We carried out a dose test experiment to find out the optimum conditions to cut the $PdSe_2$ film. We studied both 3.5 mW and 7.8 mW laser powers. However, the 3.5mW laser power does not result in complete film removal, as can be seen in Supporting information S5. Therefore, we focused on 7.8 mW laser power. To produce

homogeneous laser patterning, the scanning step size of 500 nm was selected with exposure time of 1 s per point. Figure 4 shows the results observed for different lateral step size. Raman spectroscopy confirms successful removal of the material in the regions of maximum exposure, as can be seen by absence of the $PdSe_2$ Raman peaks and much stronger Si Raman peak. This observation is consistent with SEM and AFM results, presented in Figure 4, and EDX results presented in Supporting information S6. In fact, we found out that the ribbons as narrow as 500 nm can be fabricated by this technique, demonstrating the potential for fabrication of user defined micro/nano structures in $PdSe_2$ film.

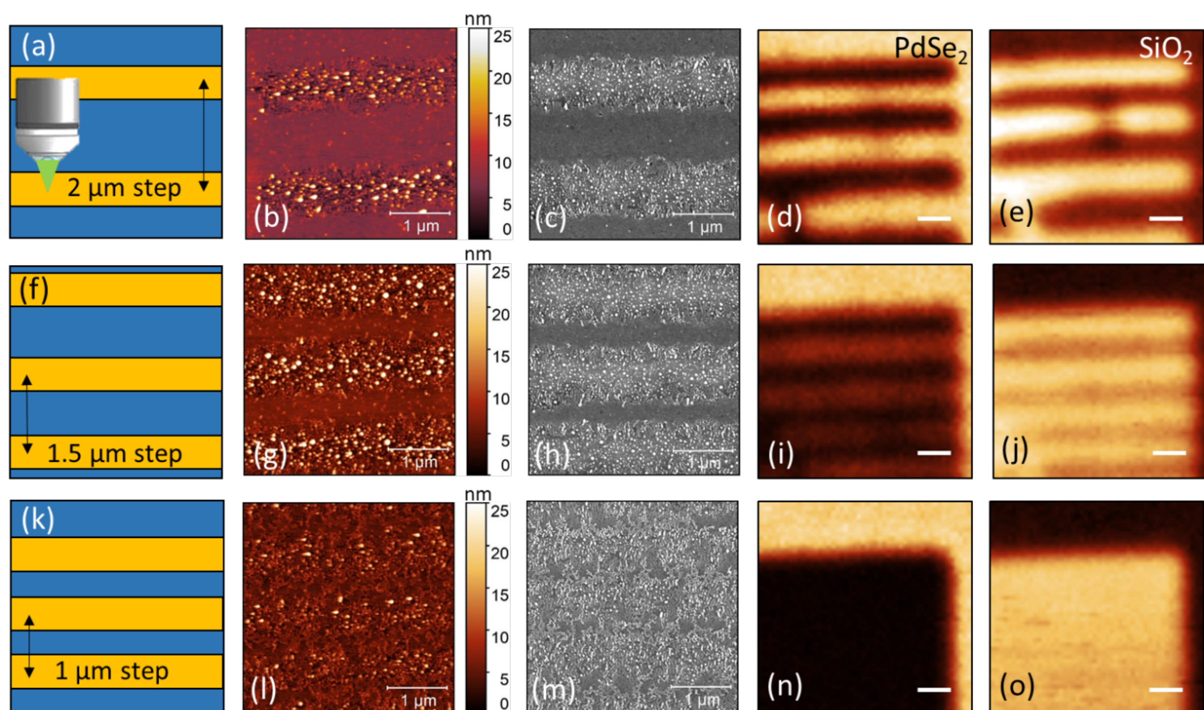

Figure 4. Laser enabled patterning of the $PdSe_2$ film. The laser power of 7.8 mW is used with 500 nm step in x direction and varying step in y direction: (a-e) 2 µm, (f-j) 1.5 µm and (k-o) 1 µm. Schematic of the patterned regions (a,f,k). AFM (b, g, l) and SEM (c, h, m) images of the patterned films. The spatial Raman maps of the area of the $PdSe_2$ peak at 260 cm^{-1} (d, i, n) and the Si peak at 520 cm^{-1} (e, j, o) measured in the laser-patterned regions. The values are in

the range of 200-400 a. u. and 2500-5500 a. u. for the $PdSe_2$ and Si peaks, respectively. Scale bar is 1 μm.

Finally, we employ the laser patterning and laser thinning techniques to demonstrate on-demand device fabrication, as schematically presented in Figure 5a. The device fabrication consisted of four steps, as outlined in Figure 5b. The $PdSe_2$ film was transferred on prepatterned graphene electrodes with defined gap of 1.2 μm (Steps (i) and (ii) in Fig. 5b). This is when the first electrical characterisation was performed. Next, the device was modified using laser exposure by the following two steps. During the first laser annealing step, the high laser power of 7.8 mW was used to locally remove the $PdSe_2$ film (Step (iii) in Fig. 5b). In this way the device channel of 6 μm was formed. During the second laser annealing step (Step (iv) in Fig. 5b), the area marked by red rectangle was laser thinned using 1.8 mW and 200 nm scanning step. Since at this laser power the modified material area is much smaller compared to 7.8 mW exposure (Fig. 3e,g), a smaller scanning step is required to produce homogenous modification of the film. The results obtained with a 500 nm scanning step show that some areas of the film remain unannealed, as confirmed by AFM and SEM results (Supporting information S7). In contrast, a 200 nm scanning step allows fabrication of a much more homogeneous film as confirmed by reduced surface roughness of 600 pm compared to 740 pm observed for a 500 nm scanning step. AFM results show that using this annealing conditions the film thickness can be reduced by ~4.1 nm (Supporting information S7). The areas of burnt $PdSe_2$ are clearly identified in optical microscopy and SEM images (Figure 5 c-e). Consistent with previous results, laser annealing at high power results in nanoparticle formation, as shown in Figure 5e. Interestingly, the underlying graphene film remains intact at this laser power, as confirmed by SEM results (Figure 5e) where graphene contact can be recognised by darker contrast. Raman spectroscopy further confirms that $PdSe_2$ film is locally removed under high laser power

exposure of 7.8 mW conditions, while graphene remains as seen by a strong 2D peak (Fig. 5 f,g).

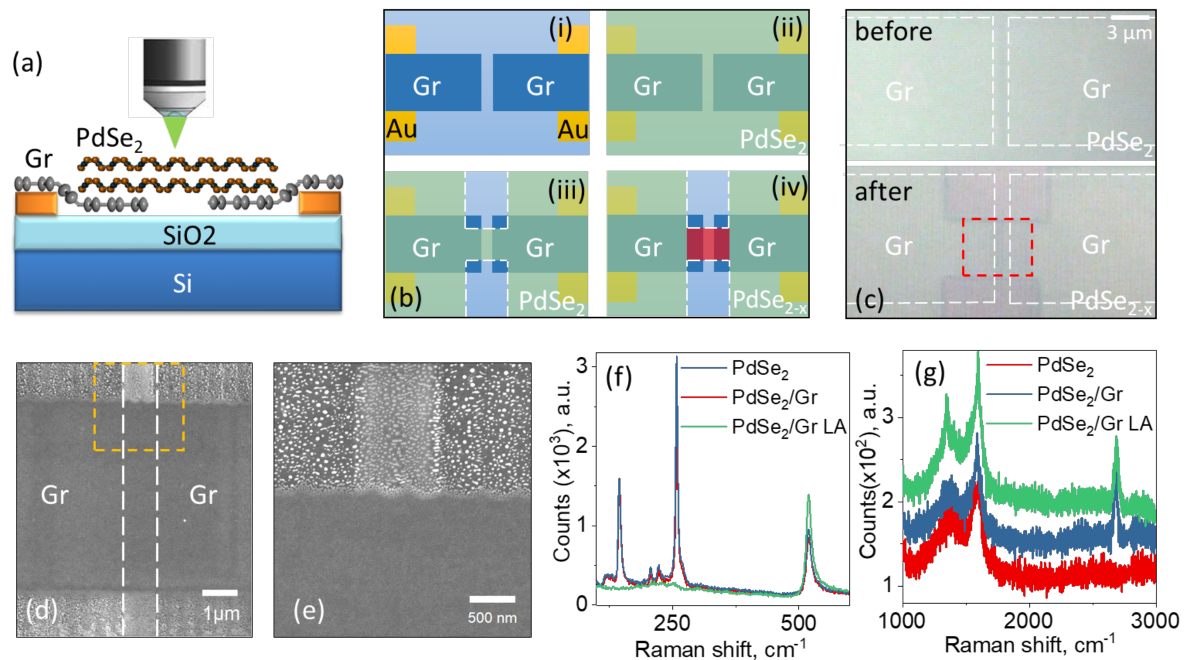

Figure 5. Laser modification of $PdSe_2$ FET device. (a) Schematic of the laser annealing of $PdSe_2$ FET devices with graphene contacts. (b) Schematic of the device fabrication process: (i) e-beam patterning of graphene electrodes with a gap of 1.2 μm on top of gold contacts, (ii) transferring of continuous $PdSe_2$ film on top of the defined graphene contacts, (iii) defining the $PdSe_2$ device channel by local removal of material with high laser power of 7.8 mW, (iv) local phase modification to create $PdSe_{2-x}$ channel with moderate laser power of 1.8 mW, the modified part is presented by red area. (c) Optical microscopy image of the device before and after laser patterning. The white dashed lines show the position of the underlying graphene contacts. The red dashed rectangular represents the area where the phase modification was performed. (d, e) SEM images of the modified area, where (e) is a zoom-in image of the yellow rectangular area in (d). (f, g) Representative Raman spectra for the $PdSe_2$ and $PdSe_2$/Gr regions before and after laser annealing with high laser power of 7.8 mW (LA).

Next, we compare the electrical properties of laser fabricated and unmodified $PdSe_2$ layers. The field effect transistors (FET) were characterised using two-terminal configuration. Figure 6a shows conductivity as a function of back gate bias (V_g) for a typical device with unmodified $PdSe_2$ film. The measured transport curve is typical of a p-doped FET. However, the device behaviour can be influenced by gate sensitivity of the graphene electrodes. In general, the fabricated device can be understood as a pair of back-to-back Schottky diodes (Figure 6g), where Schottky barriers are observed at the interface of graphene and $PdSe_2$ films and a series resistor presented by the $PdSe_2$ channel. Since graphene's conductivity is much higher compared to $PdSe_2$, the contribution of gate dependent series resistance of graphene electrodes can be considered negligible. On the other hand, the Schottky barrier can have significant contribution towards the device behaviour. However, the *Ids-Vds* characteristics show linear behaviour at low drain voltage indicating low Schottky barrier between graphene and $PdSe_2$ films (Fig. 6d). Furthermore, we observe similar transfer curves for $PdSe_2$ FET devices fabricated with only gold electrodes where no graphene is present (Supporting information S8). This observation suggests that the behaviour of the FET device with unmodified $PdSe_2$ film is governed by the $PdSe_2$ channel and its gate dependence. In this case, we can estimate the field-effect carrier mobility from the linear region using the following formula

$$\mu = \frac{d}{\varepsilon_r \varepsilon_0 V_{ds}} \frac{\partial \sigma}{\partial V_g} = \frac{L}{W} \frac{d}{\varepsilon_r \varepsilon_0 V_{ds}} \frac{\partial I_{ds}}{\partial V_g} \quad (1)$$

where *L* and *W* are the channel length and width, respectively; ε_0 and ε_r are vacuum and SiO_2 permittivity, respectively, and *d* is the SiO_2 thickness. The hole mobility of ~ 0.33 $cm^2V^{-1}s^{-1}$ is extracted for the device shown in Figure 6a. This value is significantly lower compared to the previously reported results for exfoliated $PdSe_2$ film. In fact, Chow *et al.* [29] observed the average hole mobility of ~ 7 $cm^2V^{-1}s^{-1}$ for the ultrathin $PdSe_2$ film with thickness between 7 and 17 nm, while Oyedele *et al.* [2] studied $PdSe_2$ films with a similar range of material thickness

of 2-18 nm and reported a wide variation of the hole mobility of 2.5 - 25 $cm^2V^{-1}s^{-1}$ with lower mobility registered for the thin films of 2 nm. We attribute low mobility to the porous structure of the commercial $PdSe_2$ film as can be seen in Fig. 1,2. The improved electrical properties are expected with further development of the CVD fabrication technique.

The device exhibits quite low on/off ratio of ~10, which is in contrast with previously reported results where high on-off ratio reaching up to 10^6 was demonstrated for bilayer devices. [2,31] The low on/off ratio in this work can be associated with high p-doping of the initial $PdSe_2$ film. Therefore, under the accessible back gate bias voltages, the device cannot be fully turned off and ambipolar transport cannot be reached significantly limiting on/off values. While the surface adsorbates from the fabrication process can be the source of p-doping, the low hysteresis observed in the devices suggests that this is not the major mechanism. Furthermore, Chow *et al.* demonstrated that the surface adsorbates can be easily removed by thermal annealing at 450K as confirmed by the absence of hysteresis and strong shift of the minimum conductivity point toward negative bias. [29] Therefore, we performed prolonged thermal annealing (~12h) of the $PdSe_2$/Gr devices under high vacuum at 450K. The results show no significant change in the position of the minimum conductivity point and only slight improvement of the mobility (Supporting information S9). Therefore, we conclude that the p-doping is most likely a result of CVD growth process.

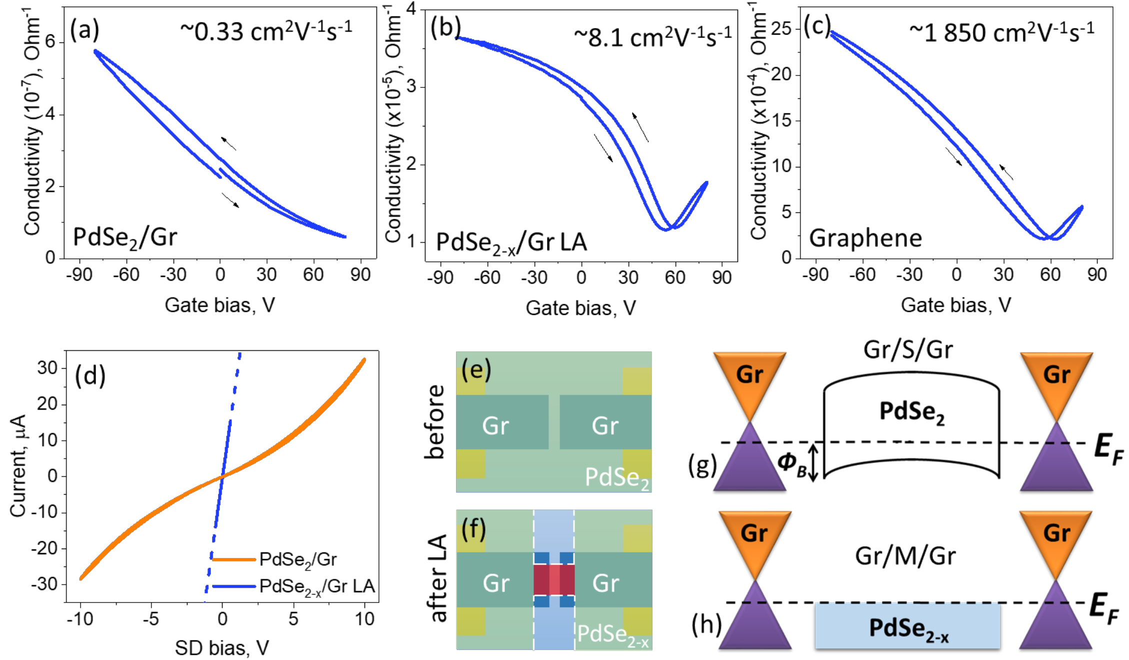

Figure 6. Electrical performance of laser modified $PdSe_2$ FET devices. (a-c) Conductivity as a function of gate voltage, measured for the unmodified ($PdSe_2$/Gr) and laser-modified ($PdSe_{2-x}$/Gr LA) $PdSe_2$ FET devices and for graphene FET device. (d) Drain-source current as a function of the drain-source voltage measured for the unmodified ($PdSe_2$/Gr) and laser-modified ($PdSe_{2-x}$/Gr LA) $PdSe_2$ FET devices. (e, f) The structural schematics for the unmodified ($PdSe_2$/Gr) and laser-modified ($PdSe_{2-x}$/Gr LA) devices and the respective energy band diagrams (g, h) depicting graphene/semiconductor (Gr/S/Gr) and graphene/metal (Gr/M/Gr) interfaces.

Next, we study the electrical characteristics of the laser fabricated device presented in Figure 5. Figure 6b shows gate dependent conductivity of the laser fabricated device. We observe two order of magnitude increase of the conductivity and 20 times improvement of hole mobility reaching 8 $cm^2V^{-1}s^{-1}$. Furthermore, in contrast with the pristine $PdSe_2$ device, the laser-fabricated FET shows the minimum conductivity point observed at 60V. This behaviour can be explained by the transition from semiconductor to metallic phase observed during laser annealing process as discussed before. Since the resistance of the $PdSe_2$ channel is strongly

reduced, it is important to consider the graphene electrode contribution to the device transport. Figure 6c shows gate dependent graphene conductivity that clearly demonstrated the charge neutrality point at 60 V. Therefore, it is possible to conclude that the behaviour of the laser fabricated device at higher gate biases (>15 V) is governed by graphene contacts. It is complicated to fully separate contributions from conductance of the $PdSe_{2-x}$ channel and the graphene contacts due to additional gate dependent junction resistances. The observed minimum conductivity point can thus be assigned to the graphene electrodes. We further confirm this by analysing the performance of $PdSe_2$ FET devices fabricated with only gold electrodes where no graphene is present. These devices show four-fold improvement in conductivity, while a minimum conductivity point is not observed (Supporting information S8). It should be noted that these devices have much larger channel lengths, limiting the possibility of uniform laser annealing. Therefore, the comparison in terms of absolute numbers can be complicated. Additionally, similar laser modification of the device channel was performed on the devices with varying gap of graphene electrodes. The results confirm strong conductivity improvement after the material modification (Supporting information S10).

Conclusion

In summary, we have demonstrated the laser-induced phase transformation of layered $PdSe_2$ to metallic phase $PdSe_{2-x}$. STEM imaging revealed that laser irradiation progressively increases the concentration of Se vacancies resulting in phase transformation and, under extreme conditions, formation of Pd nanoparticles. Using laser irradiation, the spatially selective phase conversion was achieved to produce field effect transistor devices with modified channels. Laser induced material transformation resulted in two order of magnitude increase of the conductivity and 20 times improvement of hole mobility reaching 8 $cm^2V^{-1}s^{-1}$. The proposed technique is promising for fabrication of heterophase homojunctions removing the Schottky barriers and eliminating the contact resistance. Moreover, adjusting the laser power this

technique can be used to reliably cut the material. Therefore, laser induced phase transformation is expected to enable on demand device fabrication in various geometries to facilitate next-generation electronic devices.

Methods

CVD growth of graphene. Graphene on Cu is synthesized using chemical vapour deposition (CVD) technique. The process starts with cleaning of the Cu foil through sonication in various bathes including HCl solution (2 mins), DI water (5 mins), acetone (5 mins) and isopropanol (5 min). Then the foil is placed in the reaction tube. For the flushing and graphene synthesis processes, the following gases are used: 1% methane in argon (CH_4), 25% hydrogen in argon (H_2), and 100% argon (Ar). During the flushing step performed for 30 mins, a mixture of 1000 sccm Ar, 500 sccm H_2, and 50 sccm CH_4 is used to remove any air. Then the heating step is performed where the furnace is ramped to 1060 °C with the rising speed of 50 °C/min accompanied with a flow of 600 sccm Ar and 300 sccm H_2. After the set temperature is reached, the conditions remain unchanged to perform initial Cu annealing for 1 h. The following synthesis process is performed for 1h with the flow of 600 sccm Ar, 100 sccm H_2, and 20 sccm CH_4. The reaction is terminated by removing the sample from the heating area.

Device fabrication. For the device fabrication, graphene films are transferred on a 300 nm SiO_2/Si substrate with prepatterned photolithography contacts (5 nm Cr and 35 nm Au). For this purpose, a typical wet transfer technique is used. PMMA A8 495 is spin coated on graphene/Cu at 4500 rpm for 60 s followed by baking at 180 °C for 60 s. Next, oxygen plasma is used to remove the back side graphene followed by an overnight Cu etching step in an ammonium persulfate solution (15 g/L) and a thorough rinse in DI water. The floating PMMA/graphene is scooped out using the target substrate and dried overnight in ambient

conditions. Then the sample is annealed at 180 °C for 30 mins followed by overnight bath of acetone and IPA rinse to remove PMMA layer.

The graphene contacts are defined using standard E-beam lithography (JEOL 5500 FS EBL). A two layer resist recipe is used. The first layer of PMMA A8 495 is spin coated at 4500 rpm for 60 s followed by 90 s baking at 180 °C. The second layer of negative resist maN-2403 is spin coated at 3000 rpm for 30 s followed by 90 s baking at 90 °C. Oxygen plasma is used to remove exposed graphene areas. The polymers are then removed with overnight acetone bath and IPA rinse. To ensure the graphene electrode cleanliness, the sample is annealed in vacuum for 3 h at 180 °C to remove any remaining polymer residues.

After fabrication of graphene electrodes, a $PdSe_2$ film is transferred on top to form the final device. The multilayer $PdSe_2$, purchased from 2D Semiconductors, is a CVD-grown film on sapphire substrate. To transfer the PdSe2 film, PMMA A8 495 is spin coated at 4500 rpm for 60 s followed by 60 s baking at 150 °C. Then the PMMA/$PdSe_2$ is released from the growth substrate using 1M KOH solution for 3 h followed by extensive rinse in DI water. The film is then scooped with the target substrate and dried overnight. Next the film is annealed at 150 °C for 1 h to promote adhesion with the underlying graphene electrodes. The protective PMMA layer is then removed by overnight bath of acetone followed by IPA rinse.

TEM sample fabrication. The TEM samples were prepared using similar transfer steps as described in the device fabrication section. Si_3N_4 TEM grids with arrays of circular holes were used, which also contain markers for identifying specific holes that were laser irradiated. Firstly, graphene was transferred to TEM chips followed by $PdSe_2$ transfer. It should be noted that the chips were heated to maximum temperature of 150°C with gentle ramping up/down stages to avoid potential damage of the suspended films.

Laser modification and Raman spectroscopy. Laser modification and Raman spectroscopy are performed using a LabRam Aramis Raman Spectrometer with a 532 nm laser excitation and ×100 objective lens resulting in a laser spot size of ∼500 nm.

Transmission Electron Microscopy. ADF-STEM was conducted using an aberration-corrected JEOL ARM200 STEM equipped with a JEOL corrector operated at an accelerating voltage of 80 kV located the David Cockayne Center. Dwell times of 5−20 μs and a pixel size of 0.006 nm px^{-1} was used for imaging with a convergence semi-angle of 31.5 mrad, a beam current of 44 pA, and inner-outer acquisition angles of 49.5−198 mrad.

Electrical measurements. The transport measurements are carried out using a probe station with tungsten tips. Keithley 2400 source measure units are utilised to apply source-drain and gate bias and record the resultant currents in the devices.

Supporting information

Supporting information contains the following additional results to support the main findings of the manuscript: Crystal analysis of Pd Nanoparticles; AFM measurements of the film thickness; SEM images of material degradation; SEM images of material patterning with 3.5 mW laser power; EDX data of laser patterned region; Raman spectrum of $PdSe_2$ before and after thermal annealing at 450ºC; Raman spectrum of graphene electrode; AFM and SEM measurements of the devices after laser annealing; $PdSe_2$ FET devices with gold electrodes; $PdSe_2$ FET device with laser patterned gap; FET device with $PdSe_2$/$PdSe_{2-x}$ junction; $PdSe_2$ FET device before and after thermal annealing in high vacuum at 450K for 12h; $PdSe_2$ FET device statistics; MoS_2 and WS_2 laser-induced degradation. This material is available free of charge via the Internet at http://pubs.acs.org.

Acknowledgements

J.H.W thanks the support from the European Research Council Consolidator Grant (725258).

References:

(1) Zeng, L. H.; Wu, D.; Lin, S. H.; Xie, C.; Yuan, H. Y.; Lu, W.; Lau, S. P.; Chai, Y.; Luo, L. B.; Li, Z. J.; Tsang, Y. H. Controlled Synthesis of 2D Palladium Diselenide for Sensitive Photodetector Applications. Adv. Funct. Mater. 2018, 1806878, 1–9.

(2) Oyedele, A. D.; Yang, S.; Liang, L.; Puretzky, A. A.; Wang, K.; Zhang, J.; Yu, P.; Pudasaini, P. R.; Ghosh, A. W.; Liu, Z.; Rouleau, C. M.; Sumpter, B. G.; Chisholm, M. F.; Zhou, W.; Rack, P. D.; Geohegan, D. B.; Xiao, K. $PdSe_2$: Pentagonal Two-Dimensional Layers with High Air Stability for Electronics. J. Am. Chem. Soc. 2017, 139, 14090–14097.

(3) Selb, E.; Tribus, M.; Heymann, G. Verbeekite, the Long-Unknown Crystal Structure of Monoclinic $PdSe_2$. Inorg. Chem. 2017, 56, 5885–5891.

(4) Lei, W.; Zhang, S.; Heymann, G.; Tang, X.; Wen, J.; Zheng, X.; Hu, G.; Ming, X. A New 2D High-Pressure Phase of $PdSe_2$ with High-Mobility Transport Anisotropy for Photovoltaic Applications. J. Mater. Chem. C 2019, 7, 2096–2105.

(5) ElGhazali, M. A.; Naumov, P. G.; Mirhosseini, H.; Süß, V.; Müchler, L.; Schnelle, W.; Felser, C.; Medvedev, S. A. Pressure-Induced Superconductivity up to 13.1 K in the Pyrite Phase of Palladium Diselenide $PdSe_2$. Phys. Rev. B 2017, 96, 060509.

(6) Oyedele, A. D.; Yang, S.-Z.; Feng, T.; Haglund, A. V.; Gu, Y.; Puretzky, A. A.; Briggs, D.; Rouleau, C. M.; Chisholm, M. F.; Unocic, R. R.; Mandrus, D.; Meyer, H. M.; Pantelides, S. T.; Geohegan, D. B.; Xiao, K. Defect-Mediated Phase Transformation in Anisotropic Two-Dimensional $PdSe_2$ Crystals for Seamless Electrical Contacts. J. Am. Chem. Soc. 2019, 141, 8928–8936.

(7) Lin, J.; Zuluaga, S.; Yu, P.; Liu, Z.; Pantelides, S. T.; Suenaga, K. Novel Pd_2Se_3 Two-Dimensional Phase Driven by Interlayer Fusion in Layered $PdSe_2$. Phys. Rev. Lett. 2017, 119, 016101.

(8) Zuluaga, S.; Lin, J.; Suenaga, K.; Pantelides, S. T. Two-Dimensional $PdSe_2$-Pd_2Se_3 Junctions Can Serve as Nanowires. 2D Mater. 2018, 5, 035025.

(9) Olsen, T.; Røst, E.; Grønvold, F.; Andresen, A. F.; Hoyer, E.; Spiridonov, V. P.; Strand, T. G. Phase Relationships of Palladium Selenides. Acta Chemica Scandinavica. 2008, 33a, 251–256.

(10) Takabatake, T.; Ishikawa, M.; Jorda, J. L. Superconductivity and Phase Relations in the Pd-Se System. J. Less Common Met. 1987, 134, 79–89.

(11) Okamoto, H. The Pd-Se (Palladium-Selenium) System. J. Phase Equilibria 1992, 13, 69–72.

(12) Cho, S.; Kim, S.; Kim, J. H.; Zhao, J.; Seok, J.; Keum, D. H.; Baik, J.; Choe, D.-H.; Chang, K. J.; Suenaga, K.; Kim, S. W.; Lee, Y. H.; Yang, H. Phase Patterning for Ohmic Homojunction Contact in $MoTe_2$. Science 2015, 349, 625–628.

(13) Currie, M.; Caldwell, J. D.; Bezares, F. J.; Robinson, J.; Anderson, T.; Chun, H.; Tadjer, M. Quantifying Pulsed Laser Induced Damage to Graphene. Appl. Phys. Lett. 2011, 99, 211909.

(14) Sahin, R.; Simsek, E.; Akturk, S. Nanoscale Patterning of Graphene through Femtosecond Laser Ablation. Appl. Phys. Lett. 2014, 104, 053118.

(15) Zhou, Y.; Bao, Q.; Varghese, B.; Tang, L. A. L.; Tan, C. K.; Sow, C.; Loh, K. P. Microstructuring of Graphene Oxide Nanosheets Using Direct Laser Writing. Adv. Mater. 2010, 22, 67–71.

(16) Strong, V.; Dubin, S.; El-Kady, M. F.; Lech, A.; Wang, Y.; Weiller, B. H.; Kaner, R. B. Patterning and Electronic Tuning of Laser Scribed Graphene for Flexible All-Carbon Devices. ACS Nano 2012, 6, 1395–1403.

(17) Singh, R. S.; Nalla, V.; Chen, W.; Wee, A. T. S.; Ji, W. Laser Patterning of Epitaxial Graphene for Schottky Junction Photodetectors. ACS Nano 2011, 5, 5969–5975.

(18) Castellanos-Gomez, A.; Barkelid, M.; Goossens, A. M.; Calado, V. E.; van der Zant, H. S. J.; Steele, G. A. Laser-Thinning of MoS_2: On Demand Generation of a Single-Layer Semiconductor. Nano Lett. 2012, 12, 3187–3192.

(19) Koh, Y. K.; Bae, M. H.; Cahill, D. G.; Pop, E. Heat Conduction across Monolayer and Few-Layer Graphenes. Nano Lett. 2010, 10, 4363–4368.

(20) Bae, M. H.; Ong, Z. Y.; Estrada, D.; Pop, E. Imaging, Simulation, and Electrostatic Control of Power Dissipation in Graphene Devices. Nano Lett. 2010, 10, 4787–4793.

(21) Ryu, G. H.; Zhu, T.; Chen, J.; Sinha, S.; Shautsova, V.; Grossman, J. C.; Warner, J. H. Striated 2D Lattice with Sub-nm 1D Etch Channels by Controlled Thermally Induced Phase Transformations of $PdSe_2$. Adv. Mater. 2019, 1904251, 1904251.

(22) Sun, J.; Shi, H.; Siegrist, T.; Singh, D. J. Electronic, Transport, and Optical Properties of Bulk and Mono-Layer $PdSe_2$. Appl. Phys. Lett. 2015, 107, 2–6.

(23) Mostaani, E.; Drummond, N. D.; Fal'ko, V. I. Quantum Monte Carlo Calculation of the Binding Energy of Bilayer Graphene. Phys. Rev. Lett. 2015, 115, 115501.

(24) Wang, Y.; Li, Y.; Chen, Z. Not Your Familiar Two Dimensional Transition Metal Disulfide: Structural and Electronic Properties of the PdS_2 Monolayer. J. Mater. Chem. C 2015, 3, 9603–9608.

(25) Chen, Q.; Li, H.; Zhou, S.; Xu, W.; Chen, J.; Sawada, H.; Allen, C. S.; Kirkland, A. I.; Grossman, J. C.; Warner, J. H. Ultralong 1D Vacancy Channels for Rapid Atomic Migration during 2D Void Formation in Monolayer MoS_2. ACS Nano 2018, 12, 7721–7730.

(26) Ryu, G. H.; France-Lanord, A.; Wen, Y.; Zhou, S.; Grossman, J. C.; Warner, J. H. Atomic Structure and Dynamics of Self-Limiting Sub-Nanometer Pores in Monolayer WS_2. ACS Nano 2018, 12, 11638–11647.

(27) Wang, S.; Li, H.; Sawada, H.; Allen, C. S.; Kirkland, A. I.; Grossman, J. C.; Warner, J. H. Atomic Structure and Formation Mechanism of Sub-Nanometer Pores in 2D Monolayer MoS_2. Nanoscale 2017, 9, 6417–6426.

(28) Zuluaga, S.; Lin, J.; Suenaga, K.; Pantelides, S. T. Two-Dimensional $PdSe_2$ -Pd_2Se_3 Junctions Can Serve as Nanowires. 2D Mater. 2018, 5, 035025.

(29) Chow, W. L.; Yu, P.; Liu, F.; Hong, J.; Wang, X.; Zeng, Q.; Hsu, C.-H.; Zhu, C.; Zhou, J.; Wang, X.; Xia, J.; Yan, J.; Chen, Y.; Wu, D.; Yu, T.; Shen, Z.; Lin, H.; Jin, C.; Tay, B. K.; Liu, Z. High Mobility 2D Palladium Diselenide Field-Effect Transistors with Tunable Ambipolar Characteristics. Adv. Mater. 2017, 29, 1602969.

(30) Puretzky, A. A.; Oyedele, A. D.; Xiao, K.; Haglund, A. V.; Sumpter, B. G.; Mandrus, D.; Geohegan, D. B.; Liang, L. Anomalous Interlayer Vibrations in Strongly Coupled Layered $PdSe_2$. 2D Mater. 2018, 5, 035016.

(31) Zhang, G.; Amani, M.; Chaturvedi, A.; Tan, C.; Bullock, J.; Song, X.; Kim, H.; Lien, D. H.; Scott, M. C.; Zhang, H.; Javey, A. Optical and Electrical Properties of Two-Dimensional Palladium Diselenide. Appl. Phys. Lett. 2019, 114, 253102.

TOC: